Title: Characterization of extracellular vesicles and artificial nanoparticles with four orthogonal single-particle analysis platforms

Authors:
Emily R. Mallick[1,#], emilymallick@gmail.com
Tanina Arab[1,#] ORCID 0000-0003-4485-1096, tarab1@jhu.edu
Yiyao Huang[1] ORCID 0000-0003-1749-963X, yiyaohuang@jhu.edu
Liang Dong[2] ORCID 0000-0001-7689-3237, ldong4@jhmi.edu
Zhaohao Liao[1], zliao@jhmi.edu
Zezhou Zhao[1] ORCID 0000-0003-4792-6073, zach.zhao621@gmail.com
Barbara Smith[3], bsmit112@jhmi.edu
Norman J. Haughey[4] ORCID 0000-0001-5194-4122, nhaughe1@jhmi.edu
Kenneth J. Pienta[2] ORCID 0000-0002-4138-2186, kpienta1@jhmi.edu
Barbara S. Slusher[4,5] ORCID 0000-0001-9814-4157, bslusher@jhmi.edu
Patrick M. Tarwater[6] ORCID 0000-0002-6791-1090, tarwater@jhu.edu
Juan Pablo Tosar[7,8] ORCID 0000-0002-2021-2479, jptosar@pasteur.edu.uy
Angela M. Zivkovic[9] ORCID 0000-0002-2828-7862, amzivkovic@ucdavis.edu
Wyatt N. Vreeland[10] ORCID 0000-0003-0524-8403, wyatt.vreeland@nist.gov
Michael E. Paulaitis[11] ORCID 0000-0002-9628-1091, michaelp@jhmi.edu
Kenneth W. Witwer[1,4,*] ORCID 0000-0003-1664-4233, kwitwer1@jhmi.edu

Author Information:
[1]Department of Molecular and Comparative Pathobiology, Johns Hopkins University School of Medicine, Baltimore, MD, US
[2]Department of Urology, Johns Hopkins University School of Medicine, Baltimore, MD, US
[3]Department of Cell Biology, Johns Hopkins University School of Medicine, Baltimore, MD, US
[4]Department of Neurology, Johns Hopkins University School of Medicine, Baltimore, MD, US
[5]Johns Hopkins Drug Discovery, Johns Hopkins University School of Medicine, Baltimore, MD
[6]Department of Epidemiology, Johns Hopkins University Bloomberg School of Public Health, Baltimore, MD, US
[7]Faculty of Science, Universidad de la República, Montevideo, Uruguay
[8]Functional Genomics Unit, Institut Pasteur de Montevideo, Montevideo, Uruguay
[9]Department of Nutrition, University of California Davis, Davis, CA, US
[10]Bioprocess Measurement Group, National Institute of Standards and Technology, Gaithersburg, MD, US
[11]Center for Nanomedicine at the Wilmer Eye Institute, Johns Hopkins University School of Medicine, Baltimore, MD, US

[#]These authors contributed equally to this work

***Corresponding Author:**
Kenneth W. Witwer, PhD
733 North Broadway
Miller Research Building, Room 827
Baltimore, MD 21205
Phone: 1-410-955-9770
Fax: 1-410-955-9823
Email: kwitwer1@jhmi.edu

Keywords: extracellular vesicles, exosomes, microvesicles, ectosomes, nanoparticle tracking analysis, single particle interferometric reflectance imaging sensing, resistive pulse sensing, nanoflow cytometry

ABSTRACT

We compared four orthogonal technologies for sizing, counting, and phenotyping of extracellular vesicles (EVs) and synthetic particles. The platforms were: single-particle interferometric reflectance imaging sensing (SP-IRIS) with fluorescence, nanoparticle tracking analysis (NTA) with fluorescence, microfluidic resistive pulse sensing (MRPS), and nanoflow cytometry measurement (NFCM). Results were compared with standard EV characterization techniques such as transmission electron microscopy (TEM) and Western blot (WB). EVs from the human T lymphocyte line H9 (high CD81, low CD63) and the promonocytic line U937 (low CD81, high CD63) were separated from culture conditioned medium (CCM) by differential ultracentrifugation (dUC) or a combination of ultrafiltration (UF) and size exclusion chromatography (SEC) and characterized per MISEV2018 guidelines. Mixtures of synthetic particles (silica and polystyrene spheres) with known sizes and/or concentrations were also tested. MRPS and NFCM returned similar particle counts, while NTA detected counts approximately one order of magnitude lower for EVs, but not for synthetic particles. SP-IRIS events could not be used to estimate particle concentrations. For sizing, SP-IRIS, MRPS, and NFCM returned similar size profiles, with smaller sizes predominating (per power law distribution), but with sensitivity typically dropping off below diameters of 60 nm. NTA detected a population of particles with a mode diameter greater than 100 nm. Additionally, SP-IRIS, MRPS, and NFCM were able to identify at least three of four distinct size populations in a mixture of silica or polystyrene nanoparticles. Finally, for tetraspanin phenotyping, the SP-IRIS platform in fluorescence mode and NFCM were able to detect at least two markers on the same particle. Based on the results of this study, we can draw conclusions about existing single-

79 particle analysis capabilities that may be useful for EV biomarker development and mechanistic

80 studies.

81

82

83 **INTRODUCTION**

84

85 Classification of extracellular vesicles (EVs) into subtypes has been proposed based on size,
86 biogenesis pathway, separation procedure, cellular or tissue origin, and function, among others
87 [1–6]. However, reproducible classification of EV subtypes will require single-particle
88 characterization techniques including phenotyping by surface molecules or molecular signatures
89 [7,8]. In this sense, current knowledge of EV subtypes could be compared with knowledge of
90 immune cells in the 1970s and early 1980s. Around that time, multiplexed flow cytometry
91 capabilities and cell sorting were developed, allowing more precise identification,
92 characterization, and molecular and functional profiling of immune cell subsets [9]. Single-
93 particle technologies for much smaller biological entities will be needed to divide heterogeneous
94 EV populations into well-defined and easily recognized subgroups.

95

96 In this study, we evaluated several particle types and single-particle characterization platforms.
97 For input, we used a selection of biological and synthetic particles. EVs were separated from
98 culture medium of H9 T lymphocytic cells and U937 promonocytic cells using several methods.
99 These two cell lines were chosen because they display distinct tetraspanin levels. Specifically,
100 H9 have high CD81 and low CD63 levels, while U937 produce little CD81 but abundant CD63.
101 Mixtures of distinct sizes of synthetic silica and polystyrene beads were also tested. The
102 technology platforms (Text Box 1) were: single-particle interferometric reflectance imaging
103 sensing (SP-IRIS, NanoView) [10,11] with fluorescence, nanoparticle tracking analysis (NTA,
104 ParticleMetrix) [12–14] with fluorescence, microfluidic resistive pulse sensing (MRPS,
105 Spectradyne) [14,15], and nanoflow cytometry measurement (NFCM, NanoFCM) [16,17].

106

Text Box 1: Evaluated Technologies

Single-particle interferometric reflectance imaging sensing (SP-IRIS) captures particles (*e.g.* EVs) onto a chip by affinity reagents, usually antibodies, to surface antigens. Particles are imaged by interferometric reflectance for sizing and counting, and fluorescence detection may be done for up to three channels for surface antigens or internal molecules following fixation and permeabilization. Website for the platform we used: https://www.nanoviewbio.com/

Nanoparticle tracking analysis (NTA) is an optical method to track single particles and assign sizes and counts. Measuring Brownian motion allows calculation of a hydrodynamic sphere-equivalent radius of each tracked particle. Additionally, fluorescence filters can be used for detection of particle-associated fluorescence moieties channels. Website for the platform we used: https://www.particle-metrix.de/en/particle-metrix

Microfluidic resistive pulse sensing (MRPS) counts and sizes particles as they pass through a pore between microfluidic chambers. Occlusion of the pore results in a measurable change in electrical signal (defining an event) that is proportional to the volume of the particle. Often, this technique uses different disposable cartridge pore sizes to detect particle populations within specific size ranges. As a non-optical technology, fluorescence detection is not available. Website for the platform we used: https://nanoparticleanalyzer.com/

Nanoflow cytometry measurement (NFCM) is a flow-based technique that detects nano-sized particles by scatter and/or fluorescence. Compared with traditional flow cytometry, a smaller flow channel reduces background signal, and lower system pressure increases dwell time of particles for enhanced signal integration. Website for the platform we used: http://www.nanofcm.com/products/flow-nanoanalyzer

107

108 **MATERIALS AND METHODS**

109

110 *Please see Table 1 for manufacturer, part number, and (where applicable) dilution of reagents.*

111 ***Certain commercial equipment, instruments, and reagents are identified in this paper to foster***

112 ***understanding. Such identification does not imply recommendation or endorsement by the***

113 ***National Institute of Standards and Technology or any other entity, nor does it imply that the***

114 ***materials or equipment identified are necessarily the best available for the purpose.***

115

116 **Particle Preparation:** Human cells lines H9 (T lymphocytic) and U937 (pro-monocytic) were

117 obtained from the American Type Culture Collection (ATCC). Cells were maintained in Roswell

118 Park Memorial Institute (RPMI) 1640 Medium supplemented with either replete or EV-depleted

119 10% heat-inactivated fetal bovine serum, with 1% HEPES buffer, 1% Penicillin-Streptomycin,

120 and 1% L-Glutamine. Cells were cultured at 37°C in 5% CO_2. Silica spheres (SS) were obtained

121 from NanoFCM (Nottingham, England) as a premixed combination of diameters 68 nm, 91 nm,

122 113 nm, and 151 nm. Individual polystyrene spheres (PS) were purchased at diameters 70 nm, 90

123 nm, 122 nm, and 152 nm. Equal concentrations (1×10^{12} particles/mL) of beads were mixed.

124

125 **Size Exclusion Chromatography (SEC):** 60 mL of conditioned culture medium (CCM) from

126 each cell line was centrifuged at 1,000 × g for 5 minutes at 4°C to remove cells and cellular

127 debris. 3 kDa molecular weight cut off (MWCO) Centricon Plus-70 centrifugal filters (Millipore

128 Sigma) were used to concentrate the initial volume to 1.5 mL. Size exclusion chromatography

129 (SEC) was done with qEV Automated Fraction Collectors (AFC; Izon Science, Cambridge, MA)

130 and qEV original 70 nm columns (Izon Science, Cambridge, MA). Columns were left at room

131 temperature for 30 minutes and washed with phosphate-buffered saline (PBS). EVs were loaded
132 onto the column, and 0.5 mL fractions were collected by adding additional PBS to the column.
133 EV enriched fractions (SEC; fractions 7-9) were pooled and further concentrated using 3 kDa
134 MWCO Amicon Ultra-15 Centrifugal Filters to a final volume of 1 mL. 50 µL aliquots were
135 stored at -20°C for downstream assays.
136
137 **Differential Ultracentrifugation (dUC):** 60 mL of CCM from each cell line was centrifuged at
138 1,000 × g for 5 minutes at 4°C to remove cells and cellular debris and 2,000 × g for 10 minutes at
139 4°C to remove additional debris. The supernatant was transferred to polypropylene thin-wall
140 ultracentrifugation (UC) tubes and centrifuged at 10,000 × g for 30 minutes at 4°C using a
141 swinging bucket rotor (Thermo Scientific rotor model AH-629, k-factor 242, acceleration and
142 deceleration settings of 9) to pellet large EVs. Supernatant was transferred into new
143 polypropylene thin wall UC tubes and centrifuged at 100,000 × g for 70 minutes at 4°C using the
144 same swinging bucket rotor. The 100K pellets containing small EVs were resuspended in 1 mL
145 of PBS, vigorously vortexed, and placed on ice for 20 minutes. 50 µL aliquots were stored at -
146 20°C for downstream assays.
147
148 **Transmission Electron Microscopy (TEM)**: 10 µL freshly thawed aliquots were adsorbed to
149 glow-discharged carbon-coated 400 mesh copper grids by flotation for 2 minutes. Grids were
150 quickly blotted and rinsed by flotation on 3 drops (1 minute each) of 1× Tris-buffered saline.
151 Grids were negatively stained in 2 consecutive drops of 1% uranyl acetate (UAT)
152 with tylose (1% UAT in deionized water (dIH_2O), double filtered through a 0.22 µm filter),
153 blotted, then quickly aspirated to cover the sample with a thin layer of stain. Grids were imaged

154 on a Hitachi 7600 TEM operating at 80 kV with an AMT XR80 CCD (8 megapixel). SS and PS
155 were absorbed to grids as above, but with initial flotation for 5 minutes and imaging on a Phillips
156 CM-120 TEM operating at 80 kV with an AMT XR80 CCD (8 megapixel).
157
158 **Western Blot (WB):** H9 and U937 cell pellets and isolated EVs were lysed in 1×
159 radioimmunoprecipitation assay buffer (RIPA) supplemented with protease inhibitor cocktail.
160 Protein quantification of cell and EV lysates was done using a bicinchoninic acid assay (BCA)
161 (Pierce BCA Protein Assay Kit). 5 µg of lysates were resolved using a 4% to 15% Criterion
162 TGX Stain-Free Precast gel, then transferred onto an Immuno-Blot PVDF membrane. Blots were
163 probed using primary antibodies in PBS-T and 5% Blotting Grade Blocker. Primary antibodies
164 included anti-CD81, anti-CD63, anti-CD9, anti-TSG101, anti-BiP/GRP78, and anti-GM130.
165 Rabbit anti-mouse IgGk BP-HRP and Mouse anti-rabbit IgGk BP-HRP were used as secondary
166 antibodies. SuperSignal West Pico PLUS Chemiluminescent Substrate was used for detection
167 and blots were visualized with an iBright Western Blot (Thermo Fisher, Waltham, MA) imaging
168 system.
169
170 **Single Particle Interferometric Reflectance Imaging (SP-IRIS):** Measurements were
171 performed largely as described previously [18,19]. 35 µL of H9 and U937 EVs isolated by SEC
172 or dUC were diluted 1:1 in incubation buffer (IB) and incubated at room temperature
173 on ExoView R100 (NanoView Biosciences, Brighton, MA) chips printed with anti-human CD81
174 (JS-81), anti-human CD63 (H5C6), anti-human CD9 (HI9a), and anti-mouse IgG1 (MOPC-21).
175 After incubation for 16 hours, chips were washed with IB 4 times for 3 minutes each under
176 gentle horizontal agitation at 500 rpm. Chips were then incubated for 1 hour at room temperature

177 with a fluorescent antibody cocktail of anti-human CD81 (JS-81, CF555), anti-human CD63
178 (H5C6, CF647), and anti-human CD9 (HI9a, CF488A) at a dilution of 1:1200 (v:v) in a 1:1 (v:v)
179 mixture of IB and blocking buffer. The buffer was then exchanged to IB only, followed by 1
180 wash with IB, 3 washes with wash buffer, and 1 wash with rinse buffer (3 minutes each at 500
181 rpm). Chips were immersed twice in rinse buffer for approximately 5 seconds each and removed
182 at a 45-degree angle to allow the liquid to vacate the chip. All reagents and antibodies were
183 supplied by NanoView Biosciences (Brighton, MA, Cat #EV-TETRA-C). Both SS and PS were
184 diluted in dIH_2O to load 10,000 particles, nominally, per antibody capture spot on
185 the ExoView chips. 35 µL of diluted spheres were incubated on ExoView chips and allowed to
186 fully dry. All chips were imaged in the ExoView scanner (NanoView Biosciences, Brighton,
187 MA) by interferometric reflectance imaging and fluorescent detection. Data were analyzed
188 using NanoViewer 2.8.10 Software (NanoView Biosciences). Fluorescent cutoffs were as
189 follows: CF555 channel 230, CF488 channel 475, CF647 channel 250 (biological particles) and
190 CF555 channel 675, CF488 channel 600, and CF647 channel 375 (SS and PS).
191
192 **Nanoparticle Tracking Analysis (NTA):** ZetaView QUATT-NTA Nanoparticle Tracking-
193 Video Microscope PMX-420 and BASIC NTA-Nanoparticle Tracking Video Microscope PMX-
194 120 (Particle Metrix, Inning am Ammersee, Germany) instruments were used for particle
195 quantification in both scatter and fluorescence (488 nm) modes. All calibration beads were
196 diluted using distilled water, and all samples were diluted in PBS to a final volume of 1 mL.
197 Calibration was done for both scatter and fluorescence measurements. For scatter-mode
198 calibration, 100 nm PS were diluted 1:250,000 (v:v). Capture settings were: sensitivity 65,
199 shutter 100, minimum trace length 10. Cell temperature was maintained at 25°C for all

200 measurements. For fluorescence calibration, 488 nm yellow-green FluoSpheres were diluted
201 1:250,000 (v:v), and both scatter and fluorescence were measured. Scatter was recorded as
202 above, and fluorescence was measured at sensitivity 80, shutter 100, and minimum trace length
203 15. For H9 and U937 EVs isolated by SEC or dUC, one cycle was performed by scanning 11 cell
204 positions. Capture was done at medium video setting corresponding to 30 frames per position.
205 PE-conjugated mouse anti-human CD81 and AF488-conjugated mouse anti-human CD63 were
206 used for fluorescence detection of EVs. Antibodies were mixed 1:9 (v:v) with PBS, incubated 2
207 hours at room temperature, and diluted to a final volume of 1 mL. For SS and PS mixtures,
208 samples were diluted such that at least 200 particles could be counted per frame. Technical
209 triplicates were measured for each sample. A washing step was done between each measurement
210 using dIH_2O. ZetaView Software 8.5.10 was used to analyze the recorded videos with the
211 following settings: minimum brightness 30, maximum brightness 255, minimum area 10, and
212 maximum area 1000. Supplementary Table 1 lists all antibodies tested with this platform.
213
214 **Microfluidic Resistive Pulse Sensing (MRPS):** Microfluidics resistive pulse sensing
215 measurements were conducted using the nCS1 instrument (Spectradyne, Torrance, CA) as
216 described previously [18]. Sample volumes of a few µL of H9 and U937 EVs isolated by SEC or
217 dUC were diluted with an equal volume of 1% polysorbate 20 (Tween 20) in 1× PBS (PBST)
218 and further diluted with 1× PBS, and loaded onto polydimethylsiloxane cartridges (diameter
219 range 65 nm to 400 nm). Approximately 5 µL of the diluted sample was used and about 25,000
220 events were recorded for each analyte. SS and PS were diluted 100-fold by volume in dIH_2O,
221 then 10-fold by volume with equal volumes of PBST and the remainder with 1× PBS and loaded
222 onto TS-400 polydimethylsiloxane cartridges. Approximately 3,000 events were obtained for

223 each SS and PS repeat. All acquired results were analyzed using the nCS1 Data Analyzer
224 (Spectradyne, Torrance, CA). For all samples, user-defined filtering was applied by defining 2D
225 polygonal boundaries based on transition time and diameter to exclude false positive signals,
226 similar to gating commonly used in analyzing flow cytometry data.
227
228
229 **Nano-Flow Cytometry Measurement (NFCM):** The nFCM flow nano-Analyzer was used to
230 measure concentration and size of particles following the manufacturer's instructions and as
231 described previously [20]. Briefly, two single photon-counting avalanche photodiodes (APDs)
232 were used for the simultaneous detection of side scatter (SSC) and fluorescence of individual
233 particles. The instrument was calibrated separately for concentration and size using 200 nm PE-
234 and AF488 fluorophore-conjugated PS beads and a Silica Nanosphere Cocktail, respectively.
235 20 µL of each EV preparation was incubated with 20 µL PE-conjugated CD81 and 5 µL AF488-
236 conjugated CD63 antibodies at 37°C for 30 minutes. After incubation, the mixture was washed
237 twice with PBS and centrifuged at 110,000 × g for 70 min at 4°C (TH-641 rotor, k-factor 114,
238 Thermo Fisher, using thin-wall polypropylene tubes with 13.2 ml capacity and acceleration and
239 deceleration settings of 9). The pellet was resuspended in 50 µL PBS. Events were recorded for 1
240 minute. Using the calibration curve, the flow rate and side scattering intensity were converted
241 into corresponding particle concentrations and size.
242
243

244 **Table 1**

Antibodies	**Manufacturer**	**Cat #**	**Dilution**
Primary Anti-CD81	Santa Cruz, Dallas, TX	sc-7637	1:500
Primary Anti-CD63	BD Pharmigen, San Diego, CA	556019	1:1000
Primary Anti-CD9	BioLegend, San Diego, CA	312102	1:1000
Primary Anti-TSG101	AbCam, Cambridge, MA	ab125011	1:1000
Primary Anti-BiP/GRP78	BD Pharmigen, San Diego, CA	619078	1:500
Primary Anti-GM130	AbCam, Cambridge, MA	ab52649	1:400
Secondary Mouse Anti-Rabbit IgG BP-HRP	Santa Cruz, Dallas, TX	sc-2357	1:5000
Secondary Rabbit Anti-Mouse IgGk BP-HRP	Santa Cruz, Dallas, TX	516102	1:5000
PE-Conjugated Mouse Anti-Human CD81	BD Biosciences, Franklin Lakes, NJ	555676	n/a
AF488-Conjugated Mouse Anti-Human CD63	Novus Biologicals, Littleton, CO	NBP2-42225	n/a
Reagents	**Manufacturer**	**Cat #**	
3K MWCO Centricon Plus-70	Millipore Sigma	UFC700308	
3K MWCO Amicon Ultra-15	Millipore Sigma	UFC900396	
Blotting Grade Blocker	Bio-Rad	170-6404	
Carbon Coated 400 Mesh Copper Grids	Electron Microscopy Science	CF400-Cu-UL	
Criterion TGX Stain-Free Precast Gel	Bio-Rad	5678084	
Distilled Water	Gibco	15230-162	
FluoSpheres Carboxylate-Modified Microspheres, 0.1 µm, Yellow Green Fluorescent	Thermo Scientific	F8803	
H9 Cell Line	American Type Culture Collection	HTB-176	
Heat-Inactivated Fetal Bovine Serum	GE Healthcare	SH30396.03	
Heat-Inactivated Fetal Bovine Serum, Exosome-Depleted	Gibco	A2720801	
HEPES buffer	Gibco	15630080	
Immuno-Blot PVDF Membrane	Bio-Rad	1620177	
L-Glutamine	Gibco	25030081	
Open-Top Thin Wall Ultra-Clear Tubes	Beckman Coulter	344091	
Penicillin-Streptomycin	Gibco	15140122	

Phosphatidylserine Beads	NanoFCM	S16M-Exo
Phosphate-Buffered Saline (PBS)	Gibco	14190-144
Pierce BCA Protein Assay Kit	Thermo Scientific	23225
Polypropylene Ultracentrifugation (UC) Tubes	Sorvall	03-141
Polystyrene Spheres 147 nm	Thermo Scientific	3150A
Polystyrene Spheres 125 nm	Thermo Scientific	3125A
Polystyrene Spheres 100 nm	Thermo Scientific	3100A
Polystyrene Spheres 70 nm	Thermo Scientific	3070A
Polystyrene Spheres 90 nm	Thermo Scientific	3090A
Protease Inhibitor Cocktail	Millipore Sigma	11697498001
RIPA	Cell Signaling Technology	9806
Roswell Park Memorial Institute (RPMI) 640 Medium	Gibco	11875093
Silica Nanosphere Cocktail	NanoFCM	n/a
SuperSignal West Pico PLUS Chemiluminescent Substrate	Thermo Scientific	34577
Swinging Bucket Rotor AH-629	Thermo Scientific	54284
Tris Buffered Saline (TBS)	Bio-Rad	1706435
Tween-20	Millipore Sigma	P7949
U937 Cell Line	American Type Culture Collection	CRL-1593.2
Ultra-Pure Distilled Water	Invitrogen	10977015
Uranyl Acetate	Polysciences	2144725

249 **RESULTS**

250

251 **Production, separation, and quality control of input materials**

252 Supernatants were collected from cultured human cell lines: H9 (T-lymphocytic) and U937 (pro-
253 monocytic). EVs were separated by size exclusion chromatography and ultrafiltration or
254 differential ultracentrifugation (Figure 1A). Marker expression and morphology were assessed
255 by WB (Figure 1B and Supplementary Figure 1) and TEM. WB revealed characteristic CD63
256 and CD81 expression patterns, with CD81 above the limit of detection only for H9 (Figure 1B).
257 Heterogeneous EV populations were observed by TEM in each sample preparation method
258 (Figure 1C). Additionally, we confirmed size and purity of silica spheres and polystyrene spheres
259 using TEM (Figure 1D).

260

261 **Artificial nanoparticle sizing**

262 Mixed silica spheres (SS) with nominal diameters of 68 nm, 91 nm, 113 nm, and 151 nm were
263 measured with the four platforms. Please note that since the SP-IRIS technology uses affinity to
264 capture particles, we dried particle mixtures onto the surface of the SP-IRIS chips before
265 imaging. SP-IRIS identified four distinct populations with diameter modes around 75 nm, 100
266 nm, 120 nm, and 150 nm (Figure 2A). NTA detected a broad population distribution with a mode
267 around 105 nm diameter (Figure 2B). MRPS resolved four distinct peaks for each individual
268 chip, but this distinction was masked somewhat by averaging all results (Figure 2C; see also
269 Supplementary Figure 2). NFCM resolved four populations with distinct peaks at diameters of
270 approximately 66 nm, 85 nm, 112 nm, and 154 nm (Figure 2D). Polystyrene spheres (PS) with
271 nominal diameters 70 nm, 90 nm, 122 nm, and 152 nm were mixed to a nominal concentration of
272 1×10^{12} particles/mL. SP-IRIS detected four distinct peaks around 80 nm, 110 nm, 140 nm, and

273 170 nm (Figure 2E). NTA returned a broad population distribution centered around 105 nm
274 (Figure 2F). MRPS identified distinct peaks at diameters 71 nm, 92 nm, 123 nm, and 150 nm
275 (Figure 2G). For PS, nano-flow showed four populations around 85 nm, 120 nm, 170 nm, and
276 225 nm in diameter, as well as a possible smaller population around 60 nm (Figure 2H).
277
278 **Artificial nanoparticle counting**
279 In addition to particle size, we also assessed counts. For SP-IRIS, a mean of around 3000 SS
280 particles were detected per printed antibody spot (Figure 3A), with no overall differences
281 between groups of antibody spots (*i.e.,* three spots per chip each of three tetraspanins and an
282 isotype control; note that no differences would be expected, since particles were dried onto the
283 chips). However, per-spot events overall ranged from <2000 SS particles per spot to >4500 SS
284 particles per spot (Figure 3A). SP-IRIS performed similarly for PS. There were no differences
285 between antibody groups, with a mean of around 1400 events/antibody spot (Figure 3B), but
286 events per spot ranged from <1000 PS particles/spot to 3000 PS particles/spot. Interestingly,
287 based on the nominal PS bead concentration and the surface area of the chips and spots, 10,000
288 particles per spot would be expected (Figure 3B, dotted line). Following SP-IRIS measurements,
289 chips were probed with three fluorescently labeled antibodies (anti-CD81, anti-CD63, and anti-
290 CD9) to assess background binding. Background binding was negligible for both SS and PS
291 (Supplementary Figure 3A and B, respectively). Some outliers were observed for CD9 (SS) or
292 CD63 (PS); however, none exceeded 1000 events. Particle concentrations were also measured by
293 NTA, MRPS, and NFCM. For SS (Figure 3C), MRPS estimated a concentration approximately
294 one log higher than NTA (5.1×10^{11} particles/mL *vs*. 5.4×10^{10} particles/mL, respectively), with
295 NFCM in the middle (1.7×10^{11} particles/mL). For PS, all three methods were in close agreement

296 (Figure 3D). Furthermore, the measured concentration was very close to the nominal PS
297 concentration of 1×10^{12} particles/mL (Figure 3D, dotted line).
298
299 **Biological particle sizing**
300 EV preparations from H9 and U937 cell supernatants enriched by ultrafiltration and SEC (SEC
301 EVs) or by differential ultracentrifugation (100K EVs) were next measured using each platform.
302 For H9-derived materials, SP-IRIS returned an almost identical size distribution profile for both
303 EV enrichment methods (Figure 4A). In contrast, NTA, MRPS, and NFCM measured more
304 particles at smaller diameters for the 100K EVs compared with the SEC EVs with roughly
305 similar particle size distributions (Figure 4B-D). However, substantial variation between
306 replicates might limit the conclusions that can be drawn from this observation. For U937-derived
307 materials, SP-IRIS and NTA (Figure 4E,F) detected more particles at smaller diameters from the
308 100K EVs compared with the SEC-EVs, again with roughly similar particle size distribution.
309 MRPS produced equivalent particle size distribution and particle number between the two
310 enrichment techniques (Figure 4G). In contrast, NFCM detected a higher particle count of
311 smaller particle diameters from the SEC EVs than the 100K EVs, with the particle size
312 distributions significantly different. Again, variability between replicates limits conclusions.
313 Overall, the results are broadly consistent with the reported power-law size distribution of EVs
314 [21,22] and the expectation that UC pellets may contain non-EV extracellular particles (EPs)
315 around the same size as EVs [1].
316
317 **Biological particle counting**

318 Particle counts were next assessed. As before, we present the SP-IRIS data separately because
319 this platform does not provide an overall count, but rather a number of events detected on chips
320 printed with antibodies (shown here: to CD81 and to CD63 plus an isotype control). Consistent
321 with protein assay results, SP-IRIS shows that more H9 particles were captured by anti-CD81
322 than by anti-CD63 (Figure 5A) and that U937 particles could be captured by CD63 capture
323 antibodies and not CD81 capture antibodies (Figure 5B). For the remaining three platforms,
324 which measure overall concentration, several trends were apparent (Figure 5C,D). First, for both
325 the H9 and the U937 source, and for both EV separation methods, data were consistent with the
326 results of SS counting in that NTA, NFCM, and MRPS measurements ordinally ranked from
327 lowest particles/mL to highest particles/mL. Secondly, MRPS and NFCM measured greater
328 particle concentrations for 100K EVs than for SEC EVs (corrected for processing and dilution),
329 although NTA results were similar. Finally, this is in contrast to results for the PS particles,
330 where the three techniques produced equivalent particle counts.
331
332 **Single particle phenotyping by fluorescence**
333 The SP-IRIS results represent a type of single-particle phenotyping since diameter is measured
334 for individual particles captured by antibodies and thus putatively positive for an antigen.
335 Captured particles can additionally be probed with fluorescently labeled antibodies. For chips
336 incubated with H9 EVs (Figure 6A,B), EVs captured by CD81 were generally positive for CD81
337 by fluorescence, and many also appeared to be CD63 positive. In contrast, CD63 capture spots
338 were largely devoid of fluorescence, as were (most) control capture spots. For chips incubated
339 with U937 EVs (Figure 6C,D), events on CD63 capture spots were also positive for CD63 by
340 fluorescence. CD81-linked fluorescence was at background levels for all spots. Note that
341 numbers of "positive" events are higher in fluorescence mode than with SP-IRIS (Figure 5A,B),

342 likely, as discussed later, because fluorescence detection is more sensitive than reflectance
343 imaging.
344 For the two remaining platforms with fluorescence capabilities, NTA and NFCM, results are
345 shown as percent of total particles (Figure 6E-H). Approximately 40% to 50% of detected
346 particles from H9 cells were positive for CD81 according to fluorescent NTA, while little to no
347 CD81 signal was detected for U937 materials, consistent with protein assay results. However, we
348 could not detect CD63-linked signal by fluorescent NTA for any sample. In contrast, NFCM
349 detected either CD81 or CD63 on a small percentage of particles. The percentages were similar
350 for the two tetraspanins for H9-derived particles. For U937 material, CD63-positive particles
351 were more abundant than CD81-positive particles. No major differences between the SEC and
352 100K separation methods were apparent according to these data (Figure 6E-H).
353
354

355 **DISCUSSION**

356

357 This study evaluated the abilities of four orthogonal technology platforms to size, count, and/or
358 phenotype biological EVs and synthetic nanoparticles. Three of the technologies—SP-IRIS,
359 NTA, and NFCM—are optical in nature and can perform some form of
360 phenotyping/fluorescence analysis, while the other, MRPS, is an electric sensing platform that
361 we did not attempt to apply to particle phenotyping. Although numerous comparisons of EV
362 characterization platforms have been published previously [15,23–26], this study includes
363 NFCM and MRPS and focuses in part on single-particle phenotyping.

364

365 ***Detected particles: size-range sensitivity and refractive index matter.*** Whereas NTA, MRPS,
366 and NFCM accurately and consistently measured the concentration of a known mixture of
367 polystyrene particles, estimates of the number of silica particles varied substantially. NTA
368 measured approximately 10-fold fewer SS particles than MRPS, while NFCM measured ~ 3-fold
369 fewer SS particles than MRPS. Since SS have a lower refractive index (n_{SS} ~ 1.42 [27]) than PS
370 (n_{PS} ~ 1.59 [28]), one might predict that a mixture of EVs, with an even lower refractive index
371 than silica [23,29], would have an even larger range of measurements. Indeed, for EV
372 preparations, average counts by NTA and MRPS varied by between one and two orders of
373 magnitude. These outcomes emphasize that each platform has an effective range of measurement
374 that may change with properties of particle populations, especially refractive index. Thus,
375 differences in output in part reflect different or overlapping particle populations that can be
376 detected by the specific technologies, as indeed reported previously for several of these
377 technologies [30]. That is, NTA and MRPS are similarly capable to detect a wide range of PS
378 particle sizes. However, NTA may detect a more limited range of biological particles [31] than

379 the MRPS platform using a small pore-size cartridge, in that MRPS may detect more of the
380 smaller EVs along the power-law distribution. Signal for NTA scales with radius to the 6th
381 power, whereas signal scales for MRPS with radius to the 3rd power; thus, because of finite
382 dynamic range, NTA will be biased to detecting fewer of the small particles in a sample
383 compared with MRPS.
384
385 ***Is it important to resolve different particle size populations?*** SP-IRIS, MRPS, and NFCM could
386 resolve up to four populations of synthetic nanoparticles with different diameters. We note that
387 distinct populations were somewhat obscured when MRPS results were averaged for SS, but not
388 for PS – see Supplementary Figure 4 – which may reflect aggregation of the SS due to the
389 electrolyte solution (PBS) required for MRPS and the convolution of experimental uncertainties
390 in particle concentration and size measurements. Also noteworthy is that the NFCM platform
391 distinguished subpopulations of SS particles, but that this is likely because the same beads are
392 used to calibrate the instrument. While detecting the expected concentration of high refractive
393 index PS particles, NTA was unable to resolve individual particle populations and instead
394 characterized the SS particles as a broad population distribution centered on an "average" size.
395 To be sure, it may be possible to resolve discretely sized particle populations using NTA with
396 mixtures at different ratios of sizes. We could not do so with the mixtures we used. Whether this
397 matters for biological particles is unclear. It does not seem that biological samples would contain
398 unique EV subpopulations with exquisitely defined sizes, except perhaps for samples from
399 sources infected with specific enveloped viruses. NTA does seem to be capable of detecting
400 shifts in population distributions, and this capability might be more important for biological
401 particles than resolving subpopulations.

402

403 ***On counting by SP-IRIS/fluorescence.*** One clear finding of our study is that, in our hands,
404 neither SP-IRIS label-free measurements nor subsequent fluorescence detection could be used
405 directly to estimate overall particle concentration. Instead, SP-IRIS is best used to understand
406 ratios within populations and for single-particle phenotyping. Even when PS beads were dried
407 onto chips, the measured concentration was approximately one-seventh of the expected
408 concentration. While uneven drying could contribute, it seems that PS particles non-specifically
409 adhered to the chip without a washing step, were undercounted slightly. For biological particles,
410 the problem is compounded since only a subset of EVs bind to any given affinity reagent "spot."
411 Binding is determined by diffusion (which is slow for EVs), presence and density of recognized
412 surface markers, and affinity characteristics of antibody-to-antigen binding. The bound
413 population of particles remaining after wash steps is only a miniscule proportion of the total in
414 the input material and cannot be used to determine overall concentration. Interestingly,
415 fluorescence results often indicated higher particle concentrations than returned by label-free
416 counting, even though particles positive for a particular antigen are expected to be only a subset
417 of the captured population (different antigens) or to approach equality (if the capture antigen is
418 targeted and antigen is abundant). Counts are higher because fluorescence detection is more
419 sensitive than label-free. That is, fluorescence detects positive particles that may be below the
420 limit of label-free detection.

421

422 ***Did any platforms identify differences between EV separation technologies?*** For both
423 biological sources of EVs, we used two methods of EV separation: dUC (100K EVs), which has
424 been the most common method for EV separation [32,33], and a combination of filtration and

425 size exclusion chromatography (SEC EVs) [34,35]. According to some evidence in the literature,
426 dUC leads to more protein contamination and aggregation and damage of EVs [36–38]. It should
427 be noted that alternative viewpoints can also be found [16]. However, protein particle
428 contamination might be expected to introduce more and smaller particles. This outcome is indeed
429 observed based upon TEM background and particle profile shifts towards smaller particles for
430 several of the platforms. For SP-IRIS with fluorescence, it is also interesting that tetraspanin
431 positivity is higher for samples obtained by SEC than with dUC. On the other hand, evidence of
432 aggregation by dUC is not apparent in the data presented here. We cannot rule out aggregation,
433 however, only that the techniques used here did not appear to detect it.
434
435 ***Single-particle phenotyping.*** For the three techniques with single-particle phenotyping
436 capabilities (SP-IRIS, NTA, and NFCM), each has advantages and drawbacks, as covered above,
437 all can potentially provide true single-particle phenotyping data. SP-IRIS was able to achieve the
438 most "multiplexed" detection, in that signal could be obtained above background for up to three
439 fluorescent channels. At the time of our evaluations, the NTA platform we used could not
440 perform simultaneous multi-channel measurements and thus was not a true single-particle
441 multiplexing platform. Instead, sequential filter switches were required, such that the same
442 particles could not be tracked in different channels.
443
444 In Table 2, we attempt to summarize our findings and views about the four investigated
445 techniques. **Detectable size ranges** for biological particles: these should be considered to be
446 rough estimates. If we accept the assumption that EVs follow a power-law size distribution (the
447 smaller, the more abundant, with lower bounds defined by membrane curvature constraints), then

448 no evaluated platform effectively detects the very smallest particles. However, SP-IRIS, MRPS,
449 and NFCM appear to detect slightly smaller particles than NTA under the conditions and settings
450 we tested. For NTA, MRPS, and NFCM, linear ranges for **particle concentration** for all
451 instruments begin around 1×10^7 particles/mL and extend from about one order of magnitude
452 (NTA) to multiple orders of magnitude (MRPS). This spread is important, since the wider the
453 range, the fewer time-consuming concentrations or dilutions must be done to place an unknown
454 particle population into the measurable range. SP-IRIS is a special case, since particles are
455 captured by affinity, and overall concentration cannot easily be estimated. In our hands, particle
456 concentrations must be high ($>>1\times10^7$ particles /mL) even for abundant antigens. Furthermore,
457 the optimal captured particle counts are roughly 3000 to 6000 per antibody spot (although this
458 may vary). To hit a very tight "sweet spot", many trial dilutions may be needed. Furthermore, the
459 optimal dilution may well be different for different antibodies on the chip because of different
460 percentages of EVs positive for a particular antigen, per-EV antigen abundance, and antibody
461 performance. Hence, dilutions are usually most important and time-consuming for SP-IRIS.
462 Related to dilution is the **volume of input material** required for a single reading. Assuming each
463 platform can measure 1×10^7 particles per mL, the required volume of a dilution at this
464 concentration ranges from 5 ul (MRPS) to around 1 mL (NTA). Of course, the actual
465 volume/number of EVs needed will also depend on the number of concentrations/dilutions
466 required to reach the measurable concentration range. The input volume difference is also
467 inconsequential for highly abundant materials, but may be important for low-abundance EV
468 samples. **If done, optional calibration steps** are rapid for NTA and MRPS (around 20 minutes).
469 For NFCM, we find that calibration can be as short as 20 minutes but can sometimes take longer.
470 Time for sample dilutions is most difficult to estimate, but is expected to correlate inversely with

471 the range of measurement for each platform. **Read time** ranges from five minute to about half an
472 hour per sample. Note that the times we indicate are for sizing and counting only. Optional
473 fluorescence measurements for the relevant platforms would in some cases add processing time
474 for antibody incubations and removal, as well as for read times (except for NFCM). For SP-IRIS,
475 we should also note that, although the total hands-on and read time is longer than for other
476 techniques, each reading includes on-chip replicates, multiple capture antibodies, and up to three
477 fluorescence readouts per capture antibody.
478
479 **Costs** for the platforms include initial outlay, disposable costs, and maintenance costs. For
480 acquisition, the MRPS system is most economical, while NFCM is the most expensive. For basic
481 counting and sizing, operating costs for NTA and NFCM are negligible. Adding optional
482 fluorescence increases these costs by amounts that are antibody-dependent. The MRPS system
483 uses disposable cartridges that currently cost USD 8 to USD 12 each. The SP-IRIS platform has
484 the highest disposable costs, with each sample requiring at least one chip at USD 50 to >USD
485 100 each. Since optimal dilutions are difficult to achieve and may be different for different
486 capture materials on the same chip, multiple chips may be needed for the same sample. Chips
487 also cannot be chemically stripped and re-used, at least not in our hands (Mallick and Witwer,
488 unpublished data). Furthermore, we find that chips often go unused and are thus "wasted" as a
489 result of a short shelf life of only several weeks. Since chips may take several weeks (or more for
490 custom) to procure, the three-week shelf life requires excellent planning and a lack of
491 unexpected difficulties in the laboratory; otherwise, the investment is wasted. As noted, though,
492 under optimal conditions, the platform provides multi-dimensional information that may justify
493 these costs and logistical challenges for some users. We should also mention that chips for the

494 SP-IRIS and MRPS instruments are currently available only from the instrument manufacturer
495 for that particular measurement technique. As for maintenance costs, we are unable to estimate
496 them at this time.
497
498 **In conclusion:**
499 - No evaluated platform is necessarily "better" or "worse" than others; rather, it is
500 important to be aware of the capabilities of each platform with respect to each particle
501 population of interest.
502 - Rather than relying on a single platform, consider using orthogonal technologies.
503 - Both acquisition and recurring costs should be considered before acquiring a platform.
504 Appropriate reference materials are needed for better evaluation of single particle phenotyping
505 capabilities, including multiplexed phenotyping.
506
507
508

509 **FIGURE LEGENDS**

510

511 **Figure 1: Methodology and EV separation.** (A) EVs were isolated from H9 and U937
512 conditioned cell media by a combination of ultrafiltration and size exclusion chromatography
513 (SEC EVs) or by differential ultracentrifugation (100K EVs). (B) Immunoblot analysis of
514 isolated EVs as well as corresponding cell lysates from H9 and U937 using antibodies specified
515 in Table 1; see also Supplementary Figure 1. (C) Electron microscopy images of SEC EV and
516 100K EV samples from both cell lines. Leftmost scale bars 500 nm and magnification 40 000×;
517 rightmost scale bars 100 nm and magnification 100 000×. (D) EM of SS and PS. Leftmost scale
518 bars 500 nm and magnification 17 500×; rightmost scale bars 100 nm and magnification 65
519 000×.

520

521 **Figure 2: SS and PS size distribution.** Size distributions for SS (n=3) with standard deviation
522 for (A) SP-IRIS, (B) NTA, (C) MRPS, and (D) NFCM. Nominal SS diameters are at the vertical
523 dotted lines: 68 nm, 91 nm, 113 nm, and 151 nm. Size distributions for PS (n=3; with SD) for (E)
524 SP-IRIS, (F) NTA, (G) MRPS, and (H) NFCM. Nominal PS diameters are at the vertical dotted
525 lines: 70 nm, 90 nm, 122 nm, and 152 nm. Insert in Figure 2C shows a single MRPS
526 measurement of the size distribution.

527

528 **Figure 3: SS and PS quantification.** (A) SP-IRIS label-free capture for SS and PS using four
529 capture spots (n=3 per group; mean particle count per spot with SD). B) SS quantification (n=3;
530 mean particles/mL with SD). (C) PS quantification (n=3; mean particles/mL with SD). Nominal
531 PS concentration is portrayed with a horizontal line (1.0×10^{12} particles/mL).

532

533 **Figure 4: H9 and U937 particle size distribution.** Diameters of particles for H9 SEC EVs and
534 100K EVs (n=3 per group, with standard deviation) for (A) SP-IRIS, (B) NTA, (C) MRPS, and
535 (D) NFCM. Size distributions for U937 SEC EVs and 100K EVs (n=3 per group; with SD) for
536 (E) SP-IRIS, (F) NTA, (G) MRPS, and (H) NFCM.

537

538 **Figure 5: H9 and U937 particle quantification.** SP-IRIS label-free capture for (A) H9 SEC
539 EVs and 100K EVs and (B) U937 SEC EVs and 100K EVs using CD81, CD63, and mouse
540 isotype control capture antibodies (n=3 per group; mean particle count/spot with SD). H9 and
541 U937 particle quantification (n=3; mean particles/mL with SD) for (C) SEC EVs and (D) 100K
542 EVs using NTA, MRPS, and NFCM.

543

544 **Figure 6: Particle phenotyping.** SP-IRIS fluorescence detection using labeled anti-CD81 and
545 anti-CD63 after particle capture with CD81, CD63, and mouse isotype control (n=3 per group;
546 mean and SD) for (A) H9 SEC EVs, (B) H9 100K EVs, (C) U937 SEC EVs, and (D) U937 100K
547 EVs. Percent of particles detected with fluorescently-labeled anti-CD81 and anti-CD63 by NTA
548 and NFCM (n=3 per group; mean and SD) for (E) H9 SEC EVs, (F) H9 100K EVs, (G) U937
549 SEC EVs, and (H) U937 100K EVs. Asterisk. An asterisk indicates that, in the authors' view, an
550 antibody did not perform on the instrument; it does not necessarily mean that the antibody would
551 not perform in another context or with additional optimization.

552

553 **Supplementary Figure 1: Additional EV characterization.** (A) BCA assay results, including
554 final protein concentrations in µg/mL. (B) Immunoblot analysis of separated EVs as well
555 as corresponding cell lysates from H9 and U937 using antibodies specified in Table 1.
556
557 **Supplementary Figure 2: Individual SS measurements by MRPS.** Repeats 2 (A) and 3 (B)
558 for SS using MRPS. Repeat 1 can also be found as an inset in Figure 2C.
559
560 **Supplementary Figure 3: SP-IRIS background fluorescence for SS and PS.** SP-IRIS
561 fluorescence detection using fluorescently labeled anti-CD81, anti-CD63, and anti-CD9 after (A)
562 SS and (B) PS capture with four antibody groups (n=3 per group; mean and SD).
563
564 **Supplementary Figure 4: MRPS and NFCM dilution series.** SS (A) and PS (B) were diluted
565 2×, 5×, and 10× by volume to determine the optimal dilution for NTA analysis. SS (C) were
566 diluted 1:1000 (v:v), 1:2000 (v:v), and 1:4000 (v:v) and PS (D) were diluted 1:2500 (v:v),
567 1:5000 (v:v), and 1:10000 (v:v) to determine the optimal dilution for NFCM analysis. Dilution-
568 corrected counts are for SS (E) and PS (F) on MRPS and SS (G) and PS (H) on NFCM. Optimal
569 dilutions are indicated by green or yellow (MRPS and NFCM, respectively).
570
571 **Supplementary Table 1: Antibodies tested with fluorescent NTA.** H9 100K EVs were diluted
572 1:1 (v:v) in PBS. 9 µL of diluted EVs were mixed with 1 µL of antibody and incubated for 2
573 hours at room temperature. Samples were then diluted 1:1000 and measured in scatter and
574 fluorescent modes using NTA.
575

576
577

578 **Acknowledgements:**

579 The authors thank members of the Witwer and Retrovirus Laboratories and various members of
580 the International Society for Extracellular Vesicles for discussions and support. The Authors
581 acknowledge NanoView Biosciences, Particle Metrix, Spectradyne, and NanoFCM
582 representatives for discussions and for arranging demonstrations. Electron microscopy images
583 were acquired in the Johns Hopkins University School of Medicine Institute for Basic
584 Biomedical Sciences Microscope Facility.

585

586 **Disclosure Statement:**

587 Authors report no conflicts of interest.

588

589 **Funding:**

590 This work was supported in part by the National Institute on Drug Abuse (NIDA; R01DA040385
591 and R01DA047807), the National Institute of Mental Health (NIMH; R21MH118164), The
592 National Institute of Allergy and Infectious Diseases (NIAID, R01AI144997), the National
593 Cancer Institute (NCI) and Office of the Director (UG3CA241694) and the Michael J. Fox
594 Foundation (MJFF; Grant 00900821).

595

596 **REFERENCES**

597

598 [1] Théry C, Witwer KW, Aikawa E, et al. Minimal information for studies of extracellular
599 vesicles 2018 (MISEV2018): a position statement of the International Society for
600 Extracellular Vesicles and update of the MISEV2014 guidelines. J Extracell Vesicles
601 2018;7:1535750.
602 [2] Yáñez-Mó M, Siljander PR-M, Andreu Z, et al. Biological properties of extracellular
603 vesicles and their physiological functions. J Extracell Vesicles 2015;4:27066.
604 [3] Witwer KW, Théry C. Extracellular vesicles or exosomes? On primacy, precision, and
605 popularity influencing a choice of nomenclature. J Extracell Vesicles 2019;8:1648167.
606 [4] Cocucci E, Meldolesi J. Ectosomes and exosomes: shedding the confusion between
607 extracellular vesicles. Trends Cell Biol 2015;25:364–72.
608 [5] Lázaro-Ibáñez E, Lässer C, Shelke GV, et al. DNA analysis of low- and high-density
609 fractions defines heterogeneous subpopulations of small extracellular vesicles based on
610 their DNA cargo and topology. Https://DoiOrg/101080/2001307820191656993 2019.
611 [6] Russell AE, Sneider A, Witwer KW, et al. Biological membranes in EV biogenesis,
612 stability, uptake, and cargo transfer: an ISEV position paper arising from the ISEV
613 membranes and EVs workshop. J. Extracell. Vesicles, vol. 8, Taylor and Francis Ltd.;
614 2019.
615 [7] Tkach M, Kowal J, Théry C. Why the need and how to approach the functional diversity
616 of extracellular vesicles. Philos Trans R Soc Lond B Biol Sci 2018;373:20160479.
617 [8] Lässer C, Jang SC, Lötvall J. Subpopulations of extracellular vesicles and their therapeutic
618 potential. Mol Aspects Med 2018;60:1–14.
619 [9] Lanier LL, Engleman EG, Gatenby P, et al. Correlation of functional properties of human
620 lymphoid cell subsets and surface marker phenotypes using multiparameter analysis and
621 flow cytometry. Immunol Rev 1983;74:143–60.
622 [10] Reddington AP, Trueb JT, Freedman DS, et al. An Interferometric Reflectance Imaging
623 Sensor for Point of Care Viral Diagnostics. IEEE Trans Biomed Eng 2013;60:3276–83.
624 [11] Lopez CA, Daaboul GG, Vedula RS, et al. Label-free multiplexed virus detection using
625 spectral reflectance imaging. Biosens Bioelectron 2011;26:3432–7.
626 [12] Dragovic RA, Gardiner C, Brooks AS, et al. Sizing and phenotyping of cellular vesicles
627 using Nanoparticle Tracking Analysis. Nanomedicine 2011;7:780–8.
628 [13] Sokolova V, Ludwig AK, Hornung S, et al. Characterisation of exosomes derived from
629 human cells by nanoparticle tracking analysis and scanning electron microscopy. Colloids
630 Surf B Biointerfaces 2011;87:146–50.
631 [14] Giebel B, Helmbrecht C. Methods to analyze EVs. Methods Mol. Biol., vol. 1545,
632 Humana Press Inc.; 2017, p. 1–20.
633 [15] Anderson W, Kozak D, Coleman VA, et al. A comparative study of submicron particle
634 sizing platforms: Accuracy, precision and resolution analysis of polydisperse particle size
635 distributions. J Colloid Interface Sci 2013;405:322–30.
636 [16] Tian Y, Gong M, Hu Y, et al. Quality and efficiency assessment of six extracellular
637 vesicle isolation methods by nano-flow cytometry. J Extracell Vesicles 2020;9.
638 [17] Tian Y, Ma L, Gong M, et al. Protein Profiling and Sizing of Extracellular Vesicles from
639 Colorectal Cancer Patients via Flow Cytometry. ACS Nano 2018;12:671–80.
640 [18] Ahn JY, Datta S, Bandeira E, et al. Release of extracellular vesicle miR-494-3p by ARPE-
641 19 cells with impaired mitochondria. Biochim Biophys Acta Gen Subj 2020:129598.

642 [19] Gámbaro F, Li Calzi M, Fagúndez P, et al. Stable tRNA halves can be sorted into
643 extracellular vesicles and delivered to recipient cells in a concentration-dependent manner.
644 RNA Biol 2019.
645 [20] Huang Y, Cheng L, Turchinovich A, et al. Influence of species and processing parameters
646 on recovery and content of brain tissue-derived extracellular vesicles. J Extracell Vesicles
647 2020;9:1785746.
648 [21] van der Pol E, Böing AN, Gool EL, et al. Recent developments in the nomenclature,
649 presence, isolation, detection and clinical impact of extracellular vesicles. J Thromb
650 Haemost 2016;14:48–56.
651 [22] Paulaitis M, Agarwal K, Nana-Sinkam P. Dynamic Scaling of Exosome Sizes. Langmuir
652 2018;34:9387–93.
653 [23] Van Der Pol E, Coumans FAW, Sturk A, et al. Refractive index determination of
654 nanoparticles in suspension using nanoparticle tracking analysis. Nano Lett
655 2014;14:6195–201.
656 [24] Bachurski D, Schuldner M, Nguyen PH, et al. Extracellular vesicle measurements with
657 nanoparticle tracking analysis–An accuracy and repeatability comparison between
658 NanoSight NS300 and ZetaView. J Extracell Vesicles 2019;8.
659 [25] Erdbrügger U, Lannigan J. Analytical challenges of extracellular vesicle detection: A
660 comparison of different techniques. Cytom Part A 2016;89:123–34.
661 [26] Corso G, Heusermann W, Trojer D, et al. Systematic characterization of extracellular
662 vesicles sorting domains and quantification at the single molecule–single vesicle level by
663 fluorescence correlation spectroscopy and single particle imaging. J Extracell Vesicles
664 2019;8.
665 [27] García-Santamaría F, Míguez H, Ibisate M, et al. Refractive index properties of calcined
666 silica submicrometer spheres. Langmuir 2002;18:1942–4.
667 [28] Kasarova SN, Sultanova NG, Ivanov CD, et al. Analysis of the dispersion of optical
668 plastic materials. Opt Mater (Amst) 2007;29:1481–90.
669 [29] Gardiner C, Shaw M, Hole P, et al. Measurement of refractive index by nanoparticle
670 tracking analysis reveals heterogeneity in extracellular vesicles. J Extracell Vesicles
671 2014;3.
672 [30] van der Pol E, Coumans FAW, Grootemaat AE, et al. Particle size distribution of
673 exosomes and microvesicles determined by transmission electron microscopy, flow
674 cytometry, nanoparticle tracking analysis, and resistive pulse sensing. J Thromb Haemost
675 2014;12:1182–92.
676 [31] Defante AP, Vreeland WN, Benkstein KD, et al. Using Image Attributes to Assure
677 Accurate Particle Size and Count Using Nanoparticle Tracking Analysis. J Pharm Sci
678 2018;107:1383–91.
679 [32] Théry C, Amigorena S, Raposo G, et al. Isolation and Characterization of Exosomes from
680 Cell Culture Supernatants and Biological Fluids. Curr. Protoc. Cell Biol., vol. Chapter 3,
681 Hoboken, NJ, USA: John Wiley & Sons, Inc.; 2006, p. Unit 3.22.
682 [33] Gardiner C, Di Vizio D, Sahoo S, et al. Techniques used for the isolation and
683 characterization of extracellular vesicles: results of a worldwide survey. J Extracell
684 Vesicles 2016;5:32945.
685 [34] Böing AN, van der Pol E, Grootemaat AE, et al. Single-step isolation of extracellular
686 vesicles by size-exclusion chromatography. J Extracell Vesicles 2014;3:23430.
687 [35] Théry C, Witwer KW, Aikawa E, et al. Minimal information for studies of extracellular

688 vesicles 2018 (MISEV2018): a position statement of the International Society for
689 Extracellular Vesicles and update of the MISEV2014 guidelines. J Extracell Vesicles
690 2019;8:1535750.
691 [36] Linares R, Tan S, Gounou C, et al. High-speed centrifugation induces aggregation of
692 extracellular vesicles. J Extracell Vesicles 2015;4:29509.
693 [37] Van Deun J, Mestdagh P, Sormunen R, et al. The impact of disparate isolation methods
694 for extracellular vesicles on downstream RNA profiling. J Extracell Vesicles
695 2014;3:24858.
696 [38] Arab T, Raffo-Romero A, Van Camp C, et al. Proteomic characterisation of leech
697 microglia extracellular vesicles (EVs): comparison between differential ultracentrifugation
698 and Optiprep™ density gradient isolation. J Extracell Vesicles 2019;8:1603048.
699

Figure 1. Methodology and EV separation

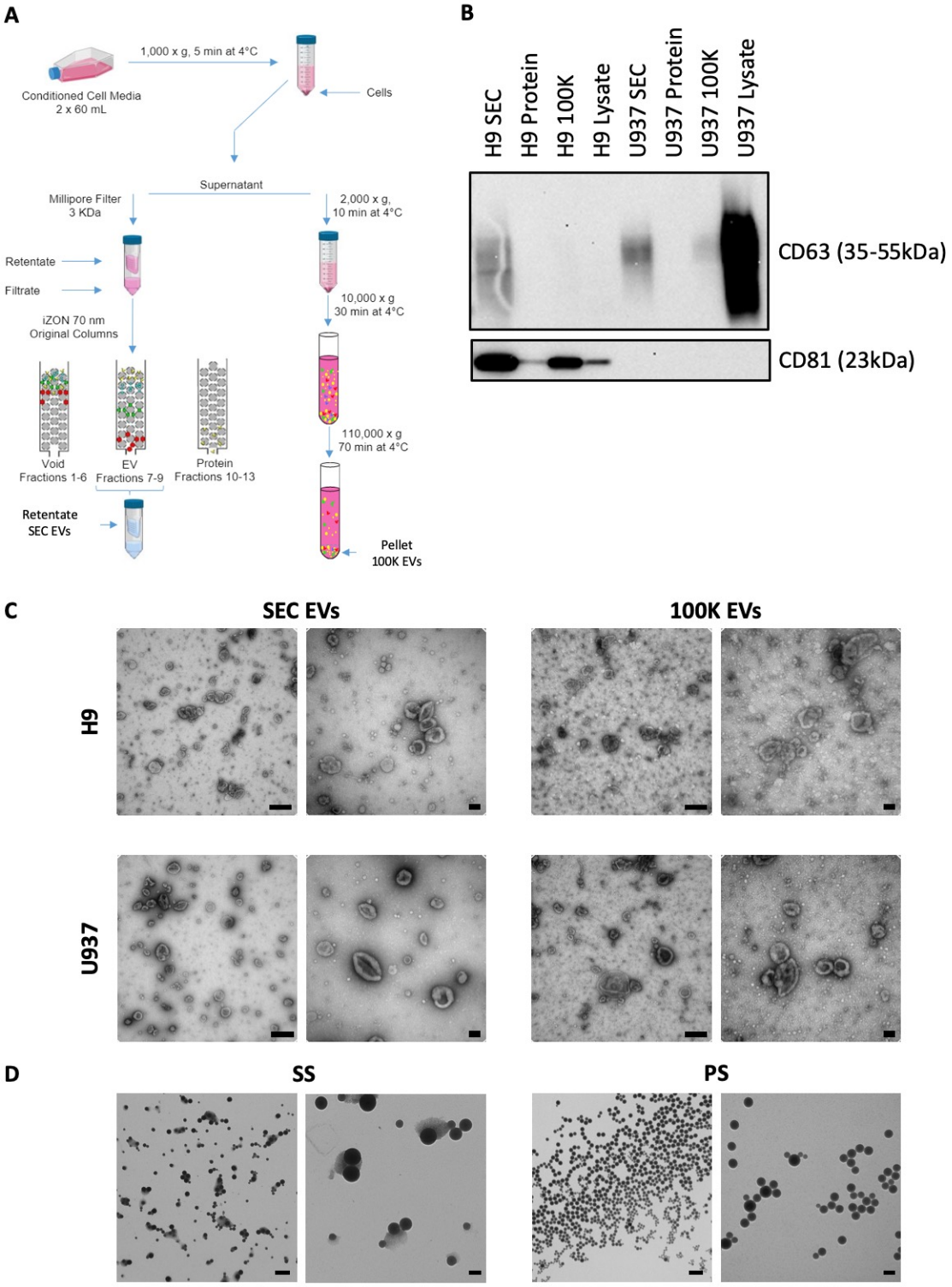

700

Figure 2. SS and PS size distribution

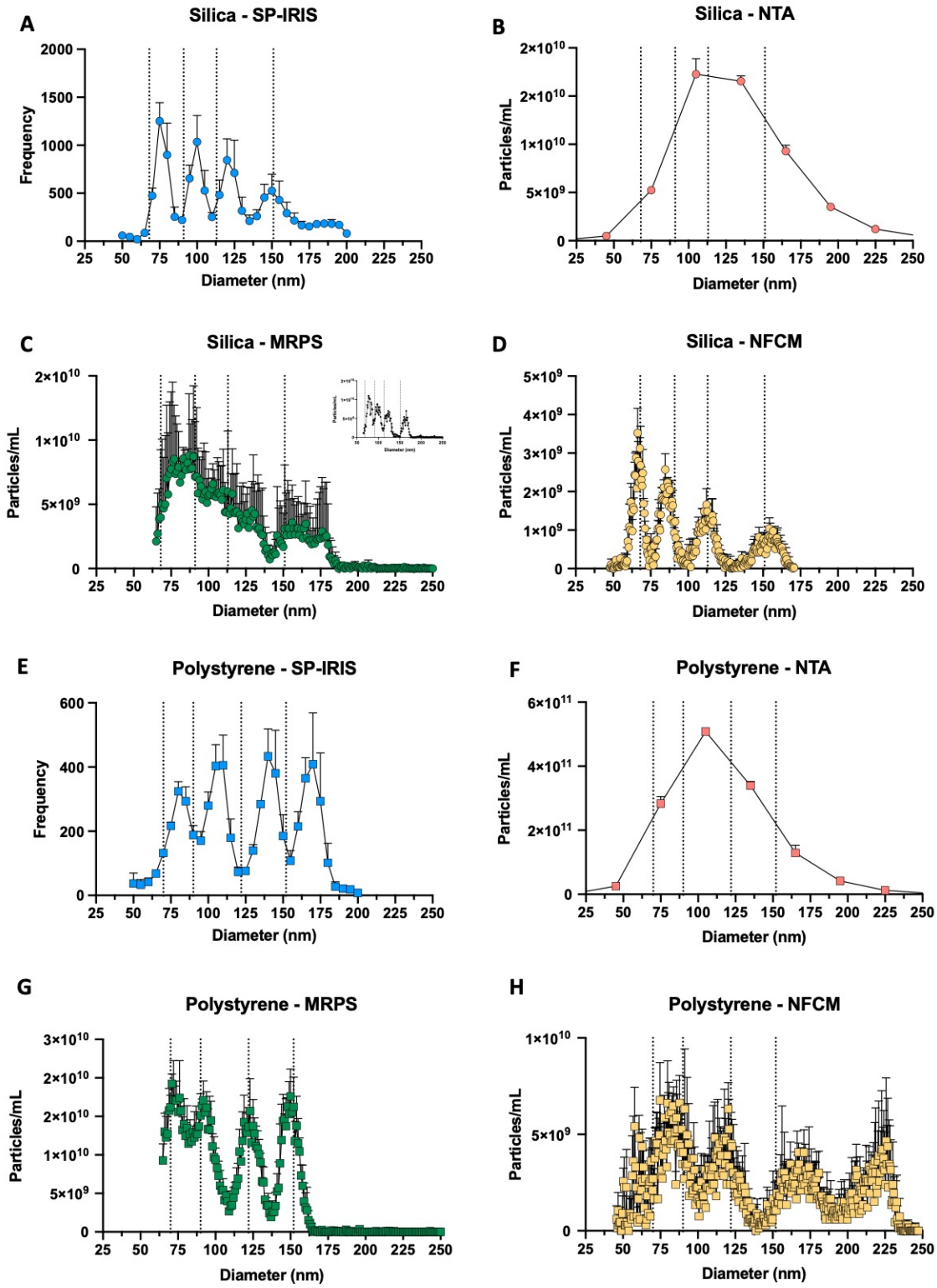

701

Figure 3. SS and PS quantification

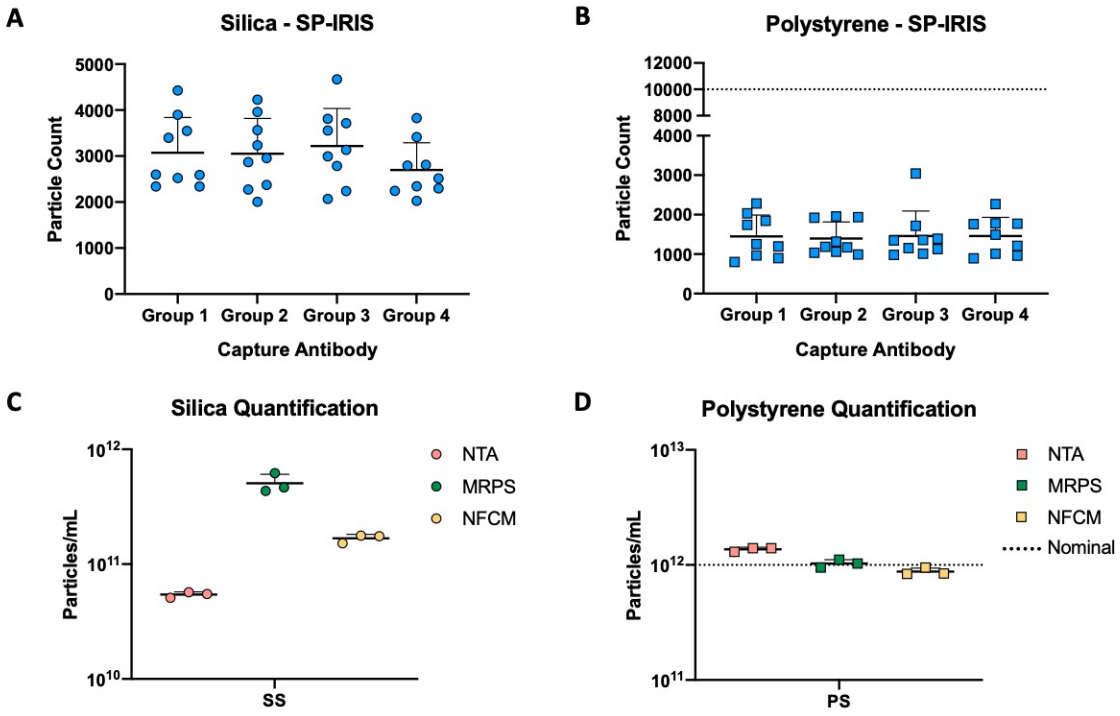

702

Figure 4. H9 and U937 Size Distribution

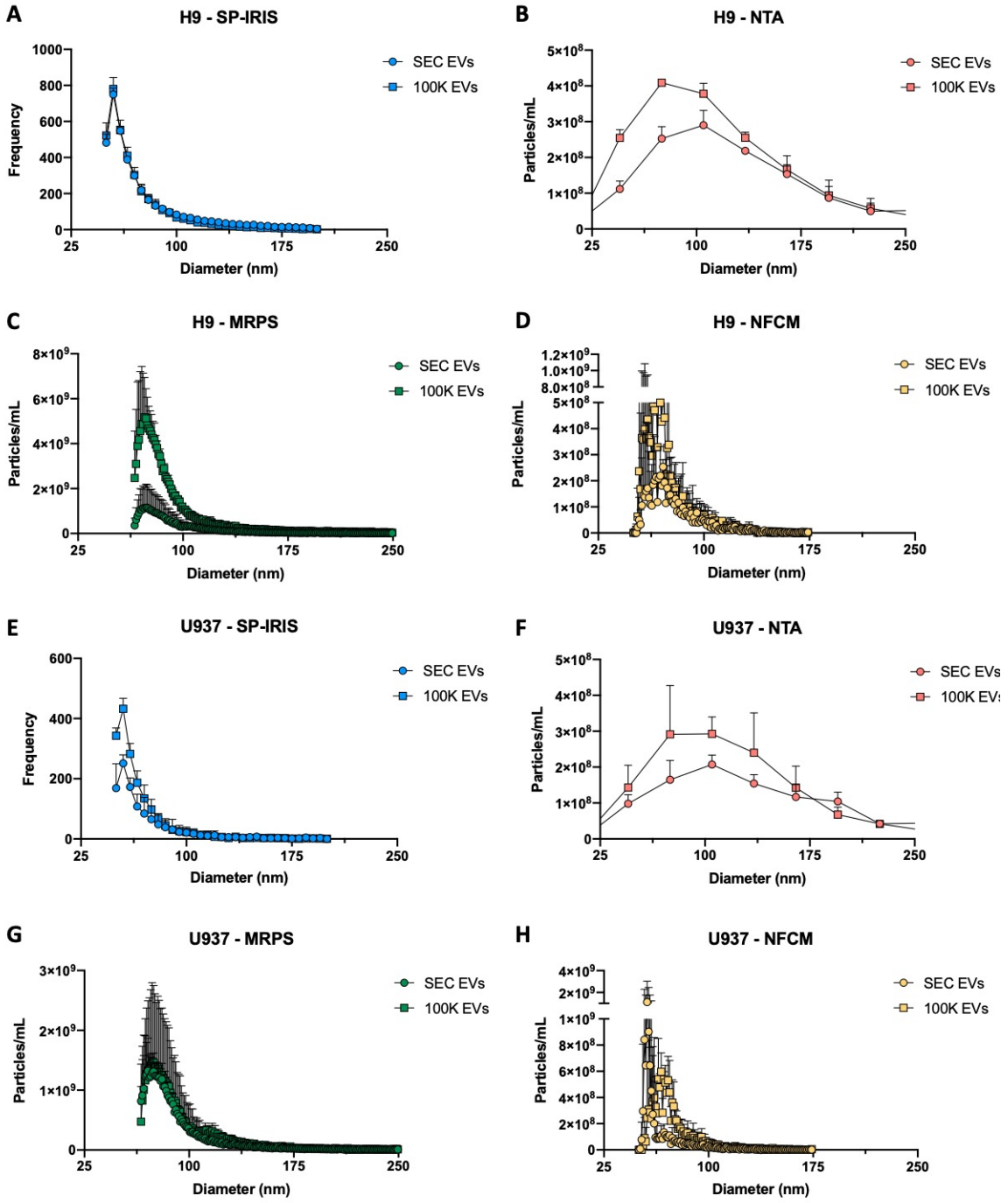

703

Figure 5. H9 and U937 particle quantification

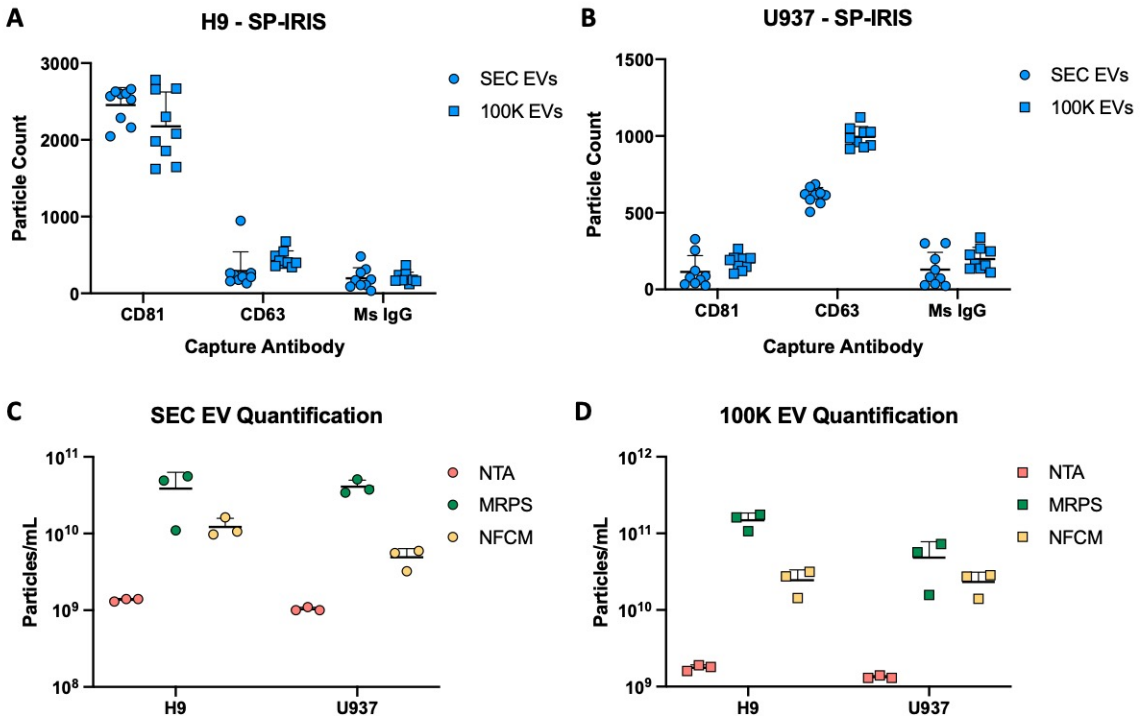

704

Figure 6. Particle phenotyping

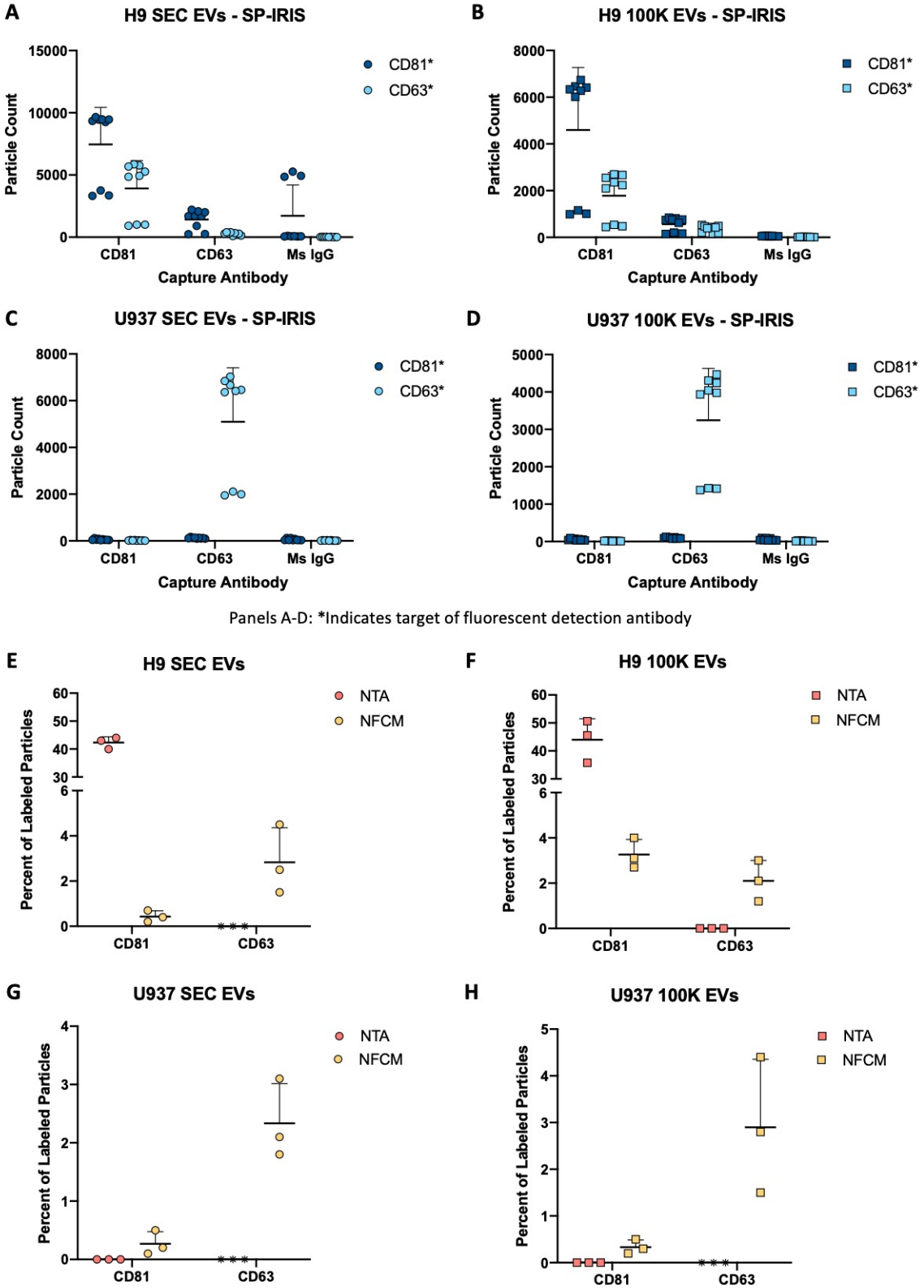

705

Table 2. Evaluation summary

Technique	Logistics						Performance		
	Estimated biological particle size detection range (diameter)	Concentration Detection Range	Input volume (µl; may be a dilution)	Operation Time: Hands-on (HO)/ Read time (R) (does not include optional labeling)	Instrument Cost	Costs for disposables	Sizing (including discrimination of different size populations)	Quantification (across all particles, biological and synthetic)	Fluorescence (channels; for instruments we evaluated)
SP-IRIS	~50 nm to 200 nm	n/a; depends on capture Ab, but >>1×10^7 particle/mL preferred	35	Day 1: 10 min sample prep (HO) Day 2: 2 hour (HO); 10 min to 30 min per sample (R)	$$	$$$: Chip/antibody kits (starting at $50/sample to >$100 for custom; ordered from manufacturer)	++	-	Up to 3
NTA	~70 nm to several hundred nm	1×10^7 to 1×10^8 particle/mL (in PBS)	1000	Optional 20 min calibration (HO/P); 5 min to 15 min per sample (HO/R)	$$	$: <$1 per sample: 1 mL syringes ($23 per 100, multiple suppliers; Ab not included)	+	+	Up to 4
MRPS	~50 nm to 2 µm (cartridge-dependent)	1×10^7 to 1×10^{10} particle /mL (in PBS/PBST)	5	Optional 20 min calibration (HO/R); 15 min to 30 min per sample (HO/R)	$	$$: Cartridges ($8 to $12 each, ordered from manufacturer)	++	++	n/a
NFCM	~40 nm to 170 nm	1×10^7 to 1×10^9 particle/mL (in PBS)	20	20 min to 120 min calibration (HO/P); 5 min per sample (HO/P)	$$$	$: <$1 per sample: 0.5 mL Tubes ($27 per 1000, multiple suppliers; Ab not included)	++	++	Up to 2

RI = refractive index; p/mL = particles per milliliter; Price range: $$$ > $$ > $; values in USD;
Performance indicator: +++ > ++ > + > -

706

Supplementary Figure 1. Additional EV characterization

A

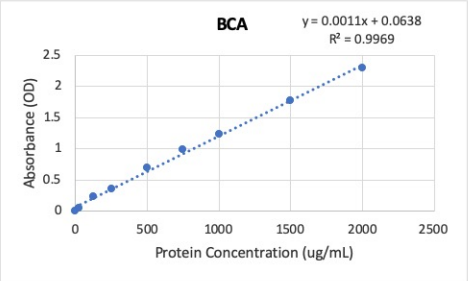

Sample	Protein Concentration (ug/mL)
H9 SEC	762.42
H9 Protein	1547.27
H9 100K	2013.94
H9 Cell lysate	3941.21
U937 SEC	550.30
U937 Protein	1762.42
U937 100K	1747.27
U937 Cell lysate	6320.00

B

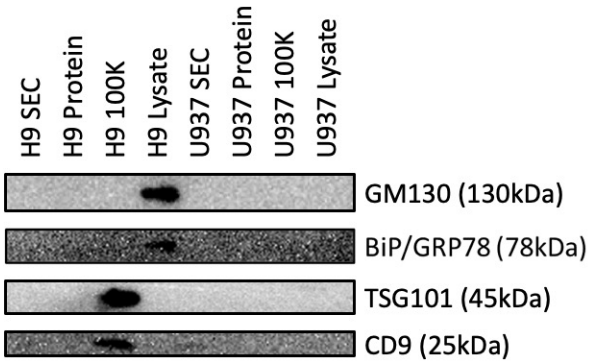

707

Supplementary Figure 2. Individual SS measurements by MRPS

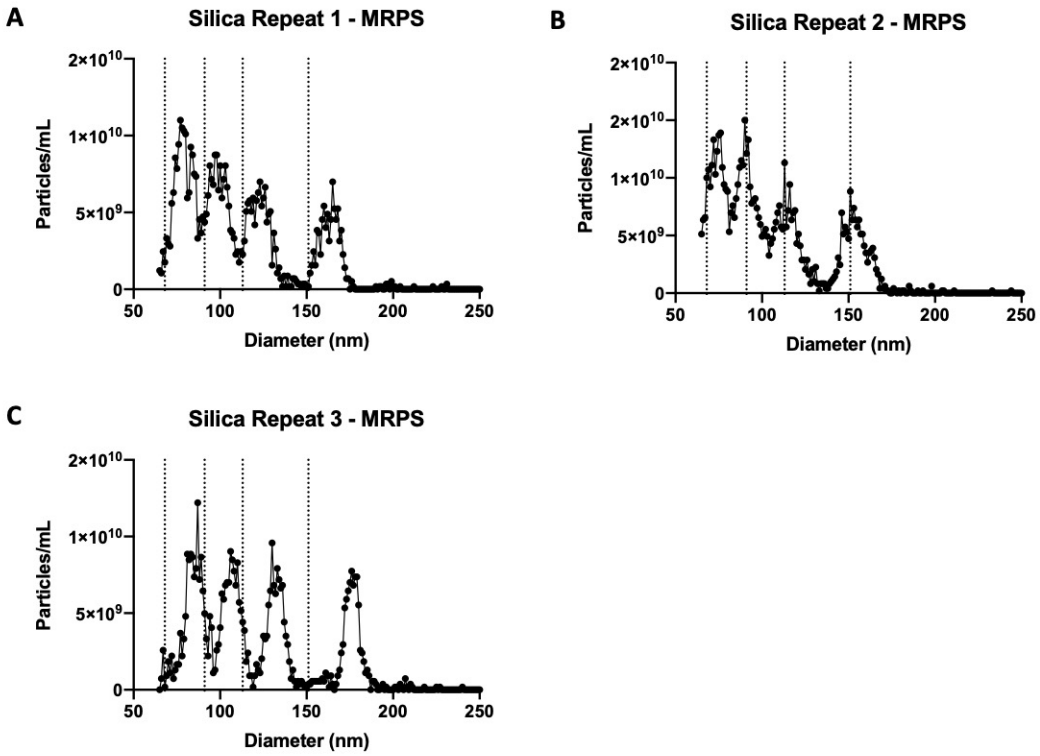

708

Supplementary Figure 3. SP-IRIS background fluorescence for SS and PS

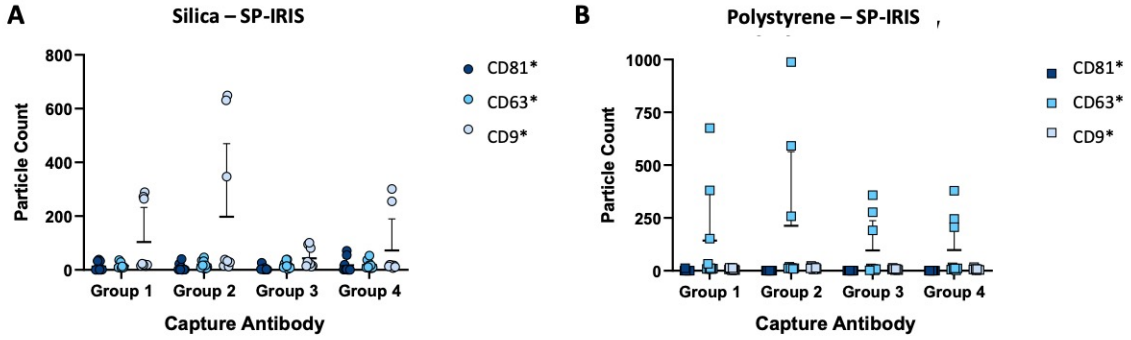

*Indicates target of fluorescent detection antibody

709

Supplementary Figure 4. MRPS and NFCM dilution series

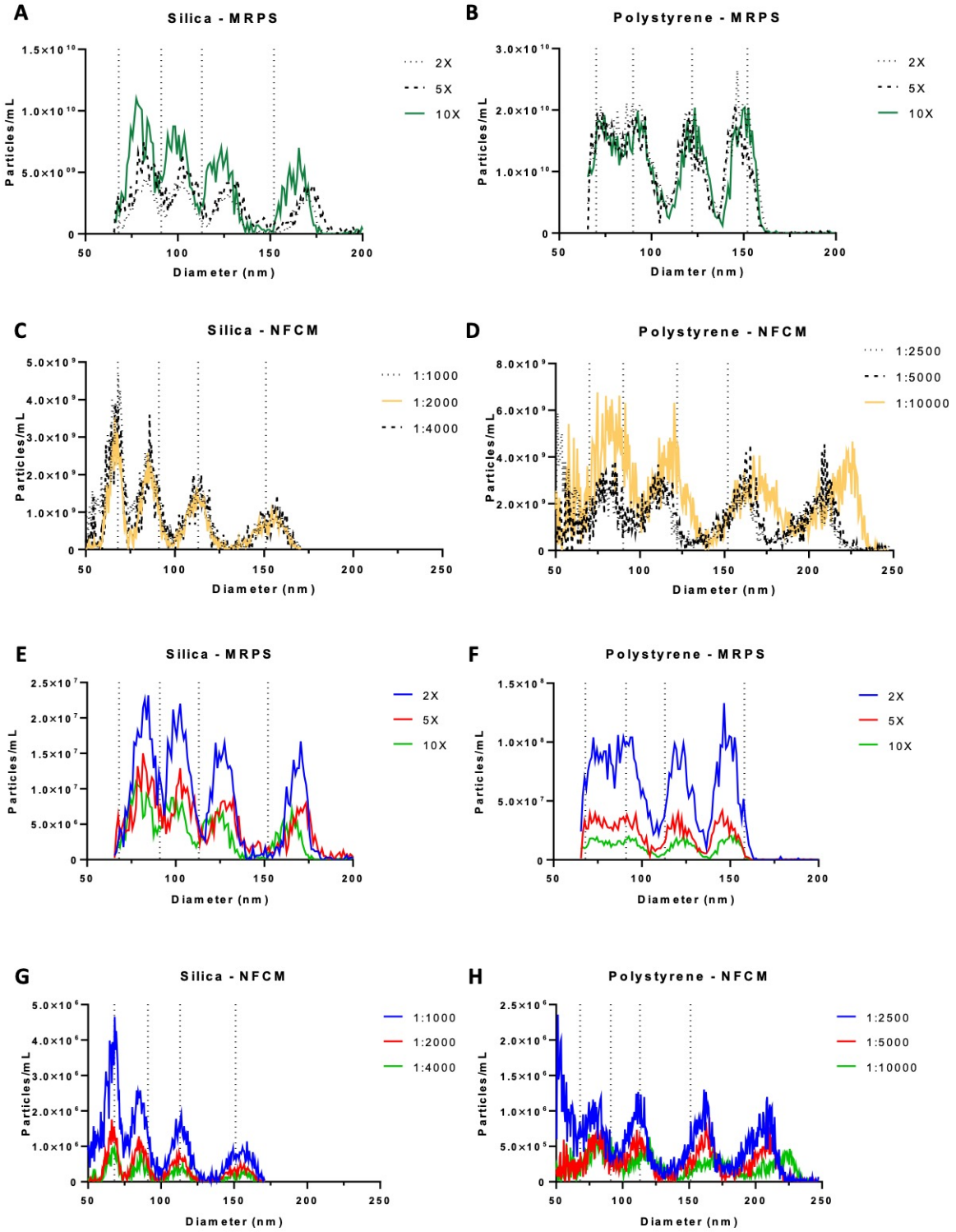

710

Supplementary Table 1. Antibodies tested with fluorescent NTA

Tetraspanin	Fluorophore	Manufacturer	Catalog Number	Signal
CD81	AF488	Santa Cruz	sc-166029	No
	PE	BD Biosciences	BDB555676	Yes
	PerCP	BD Biosciences	BDB565430	No
	APC	BD Biosciences	BDB561958	No
CD63	AF488	Santa Cruz	sc-5275	No
	AF488	Novus Biologicals	NBP2-42225	No
	PE	AbCam	ab205540	No
	V450	BD Biosciences	BDB561984	No
CD9	PE	BioLegend	312106	No
	PerCP	BD Biosciences	BDB561329	No
	FITC	AbCam	ab34162	No

711